JMEPEG (2022) 31:424–438
https://doi.org/10.1007/s11665-021-06164-7

1059-9495/$19.00

Microstructure and Mechanical Properties of Al/Cu_p/SiC_p/TiC_p-Based Hybrid Composites Fabricated by Spark Plasma Sintering

Samata Saha, Manojit Ghosh, Ashit Kumar Pramanick, Chandan Mondal, and Joydeep Maity

Submitted: 6 January 2021 / Revised: 13 July 2021 / Accepted: 20 July 2021 / Published online: 26 August 2021

Aluminum-based hybrid composites with new combinations of both hard ceramic particulates (5-10 wt.% SiC and 5-10 wt.% TiC) and ductile metallic (27 wt.% Cu) reinforcements are successfully synthesized via spark plasma sintering route to achieve significantly high specific hardness and specific modulus. The synthesized hybrid composites exhibit an adequate consolidation with marginal porosity and a clean particle–matrix interface, ensuring better particle–matrix bonding. Detailed microstructural characterization by electron microscopy and X-ray diffraction analysis further reveals that metallic copper particles could be successfully incorporated with marginal intermetallic formation by the interfacial reaction. Mechanical properties have been evaluated by macro-hardness and depth-sensing nano-indentation measurements. Among the fabricated ones, the Al-27wt.% Cu_p-5wt.%SiC_p-5wt.% TiC_p hybrid composite exhibits impressively high specific hardness (35 VHN/gcm^{-3}), specific Young's modulus (33.9 GPa/gcm^{-3}), and very high bulk modulus (28.2 GPa/gcm^{-3}) when compared with the Al-based composites reported in the literature. This is attributed to the evolution of a novel microstructure consisting of SiC, TiC, and Cu particulates in a highly sub-structured aluminum-based matrix with a significant amount of dislocation density (6.6×10^{14} m^{-2}). The elasto-plastic characteristics of the matrix are further explored through the depth-sensing nano-indentation technique.

Keywords Al-based MMCs, hardness, microstructure, nano-indentation, spark plasma sintering (SPS), transmission electron microscopy (TEM)

1. Introduction

Aluminum-based metal matrix composites (AMCs) find widespread engineering applications owing to their low density, an optimum combination of strength and ductility, impressively high thermal and electrical conductivity (Ref 1). The stir casting route has been proven to be very popular and one of the most cost-effective ways for synthesizing AMCs. However, particle segregation, clustering, interfacial reaction-induced brittle products, and micro-cracks development are some of the major challenges associated with the existing ingot metallurgy routes. In addition, the wettability issue of the particles in the molten matrix is difficult to take care of, especially with two different types of reinforcement particulates, making the synthesis of hybrid composite a complex process through the liquid metallurgy route. Conventional powder metallurgy (PM) route can overcome these constraints up to a certain extent with the added advantage of large-scale production of precision components with minimal material wastage (Ref 2). The PM route seems to be an efficient synthesis route for hybrid composite with higher material utilization, minimal machining operations, and lower energy consumption. However, higher sintering temperature coupled with longer sintering duration resulting in a coarse-grained material with inadequate strength and hardness is the key drawback of this synthesis route. Spark plasma sintering (SPS) is a comparatively new consolidation technique and is a more efficient technique than the other pre-existing consolidation techniques (Ref 2, 3) offering less sintering time and temperature, coupled with a high heating rate (Ref 2-4).

AMCs exhibit enhanced properties in terms of wear resistance, stiffness, specific strength, specific hardness, and high-temperature properties (Ref 5, 6), and hence, they are potential candidates for structural applications in aerospace, automobile industries, sports, and many more [7-10]. In the early stages of development, research efforts have been mainly focused on composites with single reinforcement. The popular reinforcements for strengthening aluminum matrix are SiC, B_4C, TiC, Al_2O_3, TiO_2, WC, etc. (Ref 7, 11). Subsequently, there has been a growing interest to develop AMCs with hybrid reinforcement encompassing the concomitant advantages of different reinforcements. In addition, the strategy culminates into a defect-enriched matrix through the exploitation of the difference in the coefficient of thermal expansion (CTE) values of different constituents (Ref 12). Song (Ref 13) has investigated the fabrication and wear properties of Al-based hybrid

Samata Saha and **Manojit Ghosh**, Department of Metallurgy and Materials Engineering, Indian Institute of Engineering Science & Technology, Shibpur, West Bengal 711103, India; **Ashit Kumar Pramanick**, MTE Division, CSIR-National Metallurgical Laboratory, Jamshedpur, Jharkhand 831007, India; **Chandan Mondal**, Rolling and Formability Group, Defence Metallurgical Research Laboratory, Kanchanbagh, Hyderabad, Telangana 500058, India; and **Joydeep Maity**, Department of Metallurgical and Materials Engineering, National Institute of Technology Durgapur, Durgapur, West Bengal 713209, India. Contact e-mails: chandan_mondal@yahoo.com and c_mondal@dmrl.drdo.in.

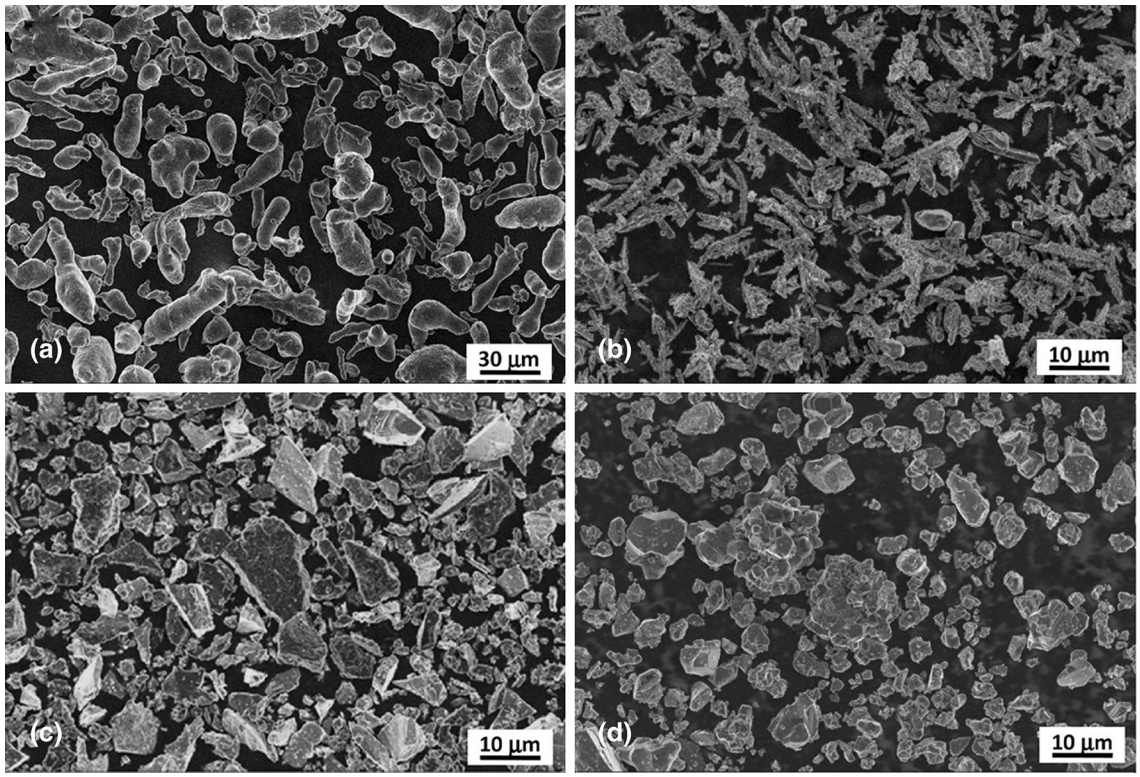

Fig. 1 SEM images showing typical morphology of initial raw materials: (a) pure Al powder, b) pure Cu powder, (c) SiC powder, and (d) TiC powder

composites with Al_2O_3 and C as reinforcements. By incorporating carbon fiber, the wear behavior has been found to improve by 20-30% compared to the AMCs with single reinforcement at the expense of tensile strength and elongation. Gupta et al. (Ref 14) have reported that the hybrid reinforcement causes a 7.6% reduction in CTE with an increase in hardness and elastic modulus by 10%, yield strength and ultimate tensile strength (UTS) by 27% for the Al-based hybrid composite with Ti particulates and iron mesh reinforcement. Oh and Han (Ref 15) have shown that the hybrid reinforcement has an excellent damage tolerance factor in addition to the low CTE value. It has been demonstrated that hybrid reinforcement of particle and short fiber is beneficial for fatigue crack growth and fracture toughness (Ref 15, 16).

From the foregoing discussion, it is clear that the Al-based composites with hybrid reinforcements have demonstrated promising properties over their mono-counterparts. However, their potential is yet to be fully realized in terms of unexplored combinations of reinforcements and novel processing routes. Therefore, the present study aims at exploring a new combination of hybrid reinforcements combined with an advanced processing route such as SPS. Synthesis of hybrid AMCs through SPS is likely to facilitate the evolution of superior microstructural attributes with enhanced mechanical properties. Accordingly, novel Al-based hybrid composites having combinations of both hard ceramic particulates (5-10 wt.% SiC and 5-10 wt.% TiC) and ductile metallic (27 wt.% Cu) reinforcements have been successfully synthesized through the SPS route for the first time. SiC is the most popular reinforcement that enhances hardness to a great extent (Ref 7, 11). On the other hand, apart from the effect on hardness enhancement, TiC is also known to enhance the modulus of elasticity significantly (Ref 17-20). Furthermore, the choice of Cu as metallic reinforcement stems from its more compatibility with matrix aluminum (being metallic and possessing a similar crystal structure). Moreover, a wide difference in the CTE of the different constituents is likely to generate a dislocation enriched matrix so as to provide a strengthening effect. Finally, the SPS route would provide maximum consolidation (low level of porosity) along with minimum degradation of microstructure. In the present article, the successful synthesis of a novel hybrid composite having enhanced hardness and modulus has been reported. The detailed microstructural evolution of three different hybrid composites has been compared along with their mechanical properties by macro-hardness and depth-sensing nano-indentation measurements. The latter technique has been utilized to demonstrate the elasto-plastic characteristics of the interfacial regions.

2. Experimental Procedure

2.1 Material and Fabrication Methods

Commercially pure Al (density: 2.7 g cm^{-3}) and Cu powders (density: 8.96 g cm^{-3}), α-SiC (hexagonal, density: 3.2 g cm^{-3}) and cubic-TiC (density: 4.92 g cm^{-3}) particulate materials were utilized as raw materials for the present study. An initial study on the morphology of the starting powders (reinforcement particulates and matrix powder) was performed as displayed in Fig. 1. The initial particle sizes of the as-received Al, Cu, SiC, and TiC powders were estimated by a particle size analyzer (Mastersizer 2000, Malvern, UK) and the average particle sizes were found to be 13, 75, 6, and 12 µm,

Table 1. Measured values of bulk and specific hardness and their correlation with dislocation density

Sample ID	Theoretical Density, g cm^{-3}	Experimental Density, g cm^{-3}	Porosity, %	Bulk hardness, VHN	Specific hardness, VHN/g cm^{-3}	Dislocation Density, m^{-2}
Pure Al	2.7	2.6985	0.05	59 ± 2 (0.579 GPa)	22	1.094×10^{14}
SRS-10	3.394	3.3706	0.69	117 ± 6 (1.147 GPa)	32.5	3.5×10^{14}
SRT-10	3.523	3.3163	5.86	78 ± 3 (0.765 GPa)	23.5	1.87×10^{14}
HYB-5	3.440	3.3566	2.42	130 ± 5 (1.275 GPa)	35.1	6.6×10^{14}

respectively. A mixture of pure Al and 30 wt.% Cu powder are ball-milled (Fritsch, PULVERISETTE classic line 6) at 300 rpm for 5 h with a ball-to-powder ratio of 10:1. The (Al+30 wt.% Cu) ball-milled powder is used to synthesize Al-based hybrid composites with Cu as ex-situ metallic reinforcement in particulate form. SiC and TiC particulates are used as ceramic reinforcements. Al-based composite powders were obtained by mixing 10 wt.% SiC, 10 wt.% TiC, and a combination of 5 wt.% SiC+ 5 wt.% TiC with the ball-milled (Al+30% Cu) powder. The composite powders so formed are designated as SRS-10, SRT-10, and HYB-5, respectively. The composite powders were consolidated using SPS technique in a Dr. Sinter 2050 equipment manufactured by Sumitomo Coal Mining Company Ltd, Japan. The sintering was carried out at a temperature of 500 °C for 8 minutes with an applied uniaxial pressure of 70 MPa. The spark plasma-sintered compacts have a diameter of 20 mm and a thickness of 5-6 mm. In addition, pure Al powder was also consolidated through SPS to compare the enhancement of properties of the unreinforced Al.

2.2 Density Measurement

The densities of the fabricated composites and SPS-compacted pure aluminum were experimentally measured by weighing small parallelepiped samples first in the air and then in water according to Archimedes' principle. The theoretical density was calculated using the rule of mixture ($\rho_{th} = \sum f_i \rho_i$ where $\mathbf{f_i}$ and $\boldsymbol{\rho_i}$ are the volume fractions and density of the constituent phases, respectively) according to the volume fraction of the metallic and ceramic reinforcements. Table 1 summarizes the experimental and theoretical density values of the composites.

2.3 Microstructural Characterization

The specimens for metallographic investigation were polished with different grades of emery papers soaked in kerosene and liquid paraffin (1:1 proportion). After the specimens were polished adequately by emery paper and then subjected to cloth polishing with fine alumina. The as-polished surfaces were rinsed in ethanol and then dried, followed by the microstructural characterization carried out using an optical microscope (Leica DM 2500 M).

The as-received individual Al and Cu powders, SiC, and TiC particulate reinforcements, as well as fabricated composites, were examined by field emission scanning electron microscopes (FESEM; Zeiss, sigma HD). Energy-dispersive X-ray spectroscopy (EDS)-based spot analysis and elemental mapping were carried out for qualitative micro-chemical analyses. Particle size (in terms of powder particle diameter) of the different constituents was determined (average powder particle diameter = mean ± standard deviation) from FESEM images considering 10 image frames. To further identify the different phases present, Al-based single reinforced and hybrid composites were subjected to X-ray diffraction (XRD) analysis at a slow scan rate (0.45° min^{-1}) in a high-resolution X-ray diffractometer (Bruker, Germany).

Thin specimens were sectioned by electrical discharge machining and were further thinned by mechanical polishing to ~60 μm thickness. Circular disk-shaped samples with a 3 mm diameter were punched and were subjected to further thinning on a dimple grinder (Gatan, USA) using diamond suspension to reduce their thickness to 30 μm. Final milling was carried out in a precision ion polishing system (Model: 691, Gatan, USA) using ~5 keV argon-ion guns with the ion beam aligned at an angle of about 3-4°. The specimens were examined under a high-resolution transmission electron microscope (Model: JEM-2100, JEOL, Japan) at an operating voltage of 200 kV. The dislocation density of the composites was estimated by using the Smith–Guttman linear intercept technique [21].

2.4 Hardness Test

Macro-hardness measurements have been carried out in a Vicker's hardness testing machine (BV 250 (S), BIE, Miraj, India) using a 30 kgf load. A minimum of five hardness readings per specimen was measured and the mean value of the hardness is reported here. Vicker's micro-hardness measurements of the different microstructural regions in the specimens were also carried out using micro-hardness testing equipment (Leica) with 50 and 200 gf loads.

2.4.1 Nano-indentation Test. Nano-indentation experiments were carried out with a micro-indentation tester (Micro-Combi tester). The indentation hardness, the bulk modulus of the specimens were measured by an instrumented recording of the applied load (P) and the penetration depth (h) simultaneously during the loading and unloading cycles. The indentations were carried out using a load of 300 mN and a holding time of 10s. By analyzing the unloading data, the hardness and Young's modulus of the material are determined.

2.5 Atomic Force Microscopy

Atomic force microscope used for the present study has the following specification: Model: SPA 400, Scanner: 20 μm scanner (with Al back coating), Cantilever: SI-DF20, Cantilever holder: DFM, Scanning Area: 20 μm and up to atomic resolution scale 2nm data type: topography, phase, non-contact force (NCF). The specimens for the AFM investigation were mirror-polished using the standard metallographic technique.

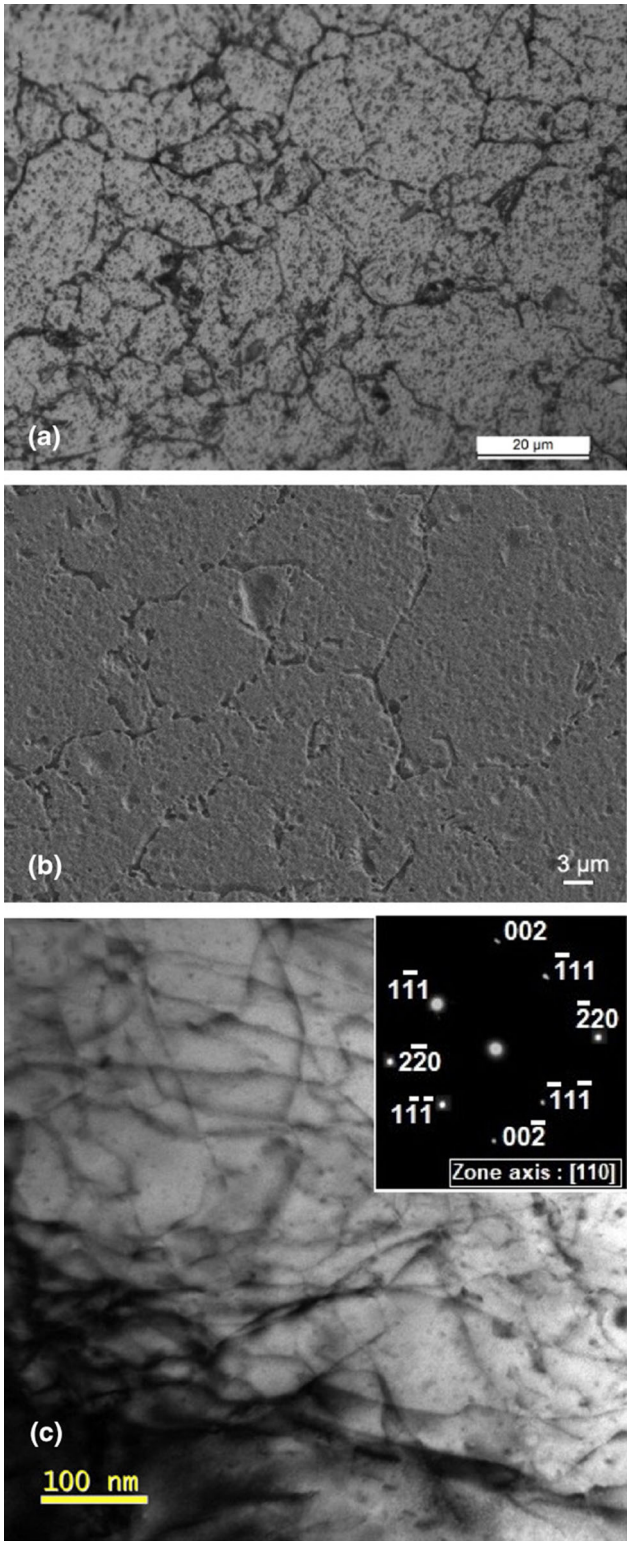

Fig. 2 Development of microstructure of SPS-consolidated pure aluminum as characterized by (a) optical microscopy, (b) SEM, and (c) TEM. (c)-inset: {110} zone axis of the matrix Al

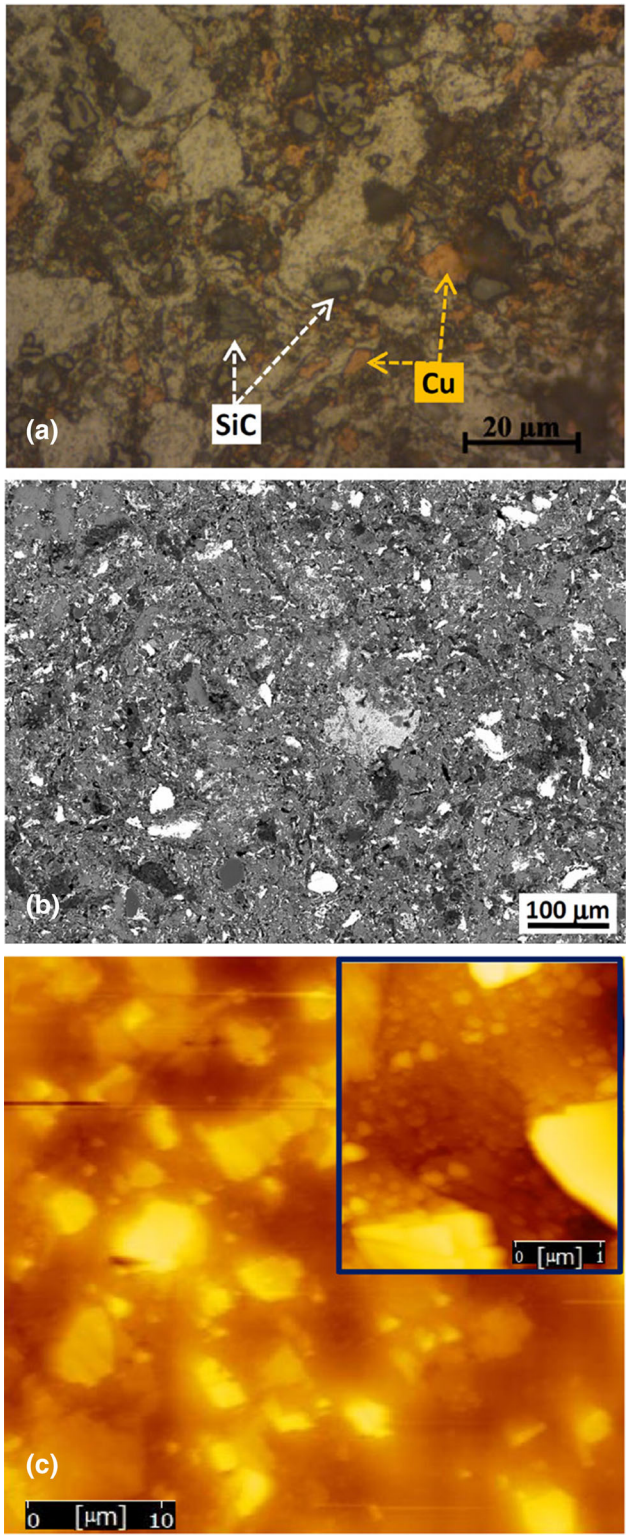

Fig. 3 (a) Optical micrograph, (b) BSE image showing the development of microstructure in SRS-10 composite. (c) AFM image revealing the distribution of particles and particle–matrix interfaces

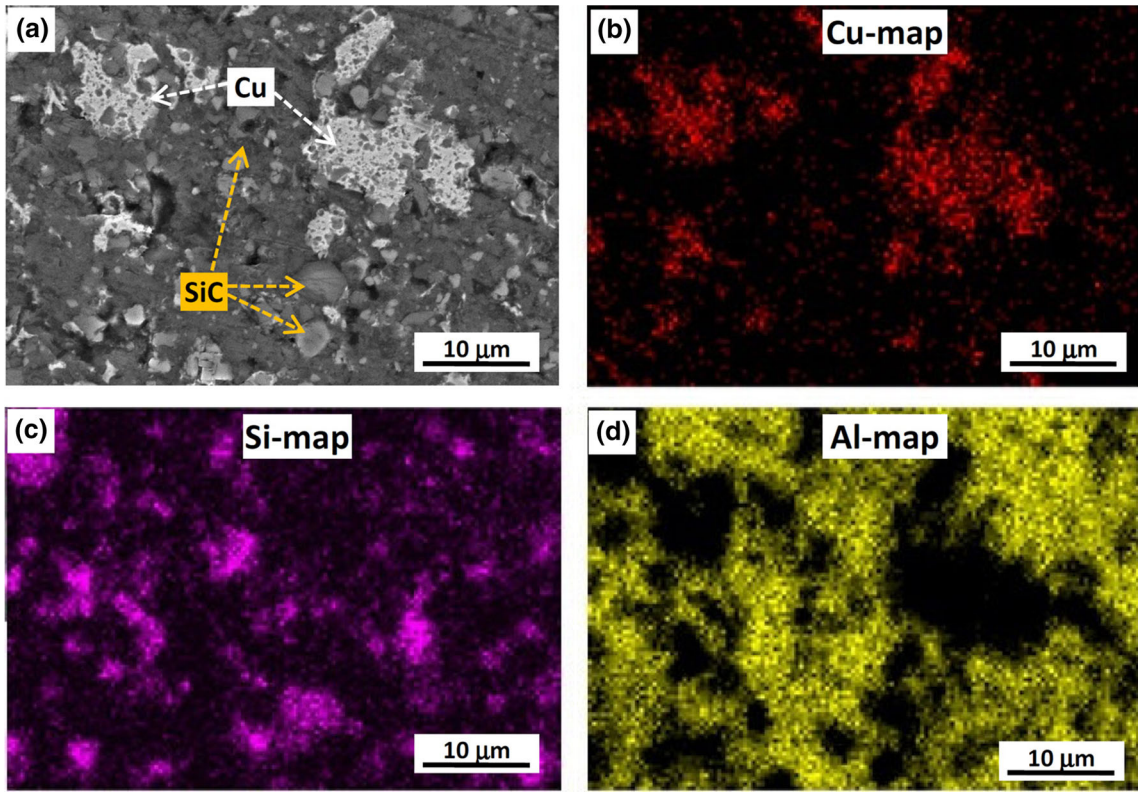

Fig. 4 (a) BSE image of the SRS-10 composite and (b)-(d) corresponding elemental maps of Cu, Si, and Al, respectively

3. Results

3.1 Microstructural Evolution

An optical micrograph of spark plasma-sintered pure Al sample exhibits a polycrystalline structure with almost equiaxed grains of Al in the matrix. Further microstructural examination with the FESEM reveals the presence of primary phases (mainly Fe-rich phases arising due to impurity content) at the grain boundaries and triple junctions (Fig. 2b). The average grain size for the pure Al compact, estimated in terms of equivalent grain diameter, is 8.37µm corresponding to the ASTM grain size number of 11. Characterization of microstructure by TEM reveals a highly sub-structured matrix consisting of dislocation network and tangles for pure Al spark plasma-sintered compact as shown in Fig. 2c. A representative selected area electron diffraction pattern (SADP) confirms the presence of FCC Al.

The optical microstructure of (Al+27wt.% Cu) +10 wt.% SiC composite (SRS-10) exhibits the uniform distribution of the ex-situ SiC particulates and in-situ intermetallic phases in the matrix (Fig. 3a). The presence of different micro-constituents revealed in the optical microstructure is also evident from the FESEM micrograph. The metallic reinforcement Cu appears as a brighter phase, whereas non-metallic SiC particulates and particle-enriched regions appeared as a darker phase in the electron micrograph (Fig. 3b). The ceramic reinforcement (i.e., SiC particles) can also be identified from their unique angular morphologies. Further microstructural examination with high magnification FESEM reveals the existence of fine spheroidal particles in the matrix and the same is confirmed from the AFM image (Fig. 3c). The brighter appearance of the fine particles in both SEM and in AFM images indicates that the spheroidal particles are based on Cu-rich equilibrium phases, identified as $CuAl_2$ and $AlCu_3$ intermetallics through X-ray diffraction analysis as demonstrated in the subsequent section. AFM micrograph also reveals the presence of these fine SiC particles that are identified from their unique angular morphology (Fig. 3c). In addition, the particle–matrix interface is distinctly visible in the AFM image (Fig. 3c: inset). It is also evident from the elemental distribution (Fig. 4) and FESEM images that along with the coarser SiC particles, extremely fine SiC particles (possibly fragmented during pressure-assisted spark plasma sintering) are distributed in the matrix. The distribution of elements and their analysis indicate that fragmented SiC particles are distributed in Cu-enriched regions.

The optical micrograph of (Al+27wt.% Cu) +10 wt.% TiC composite (SRT-10) exhibits the distribution of ex-situ TiC particles, metallic Cu reinforcements, and other fine in-situ phases (Al-Cu equilibrium phases ($CuAl_2$)) in the matrix (Fig. 5a). There are some abnormally coarse and porous TiC particles present in the matrix compared to the otherwise uniform distribution of fine TiC particles. The coarse TiC particles are presumably the clustered lumps present in the as-received powder. Some of the TiC particulates are fragmented and become finer during SPS due to applied pressures. The distributions of TiC particles and clusters are identified in the FESEM micrograph, along with some voids at the particle–matrix interface (Fig. 5c). This is also evident from the AFM image (Fig. 5d), which indicates the presence of voids at the particle–matrix interface. The presence of TiC particles and other in-situ phases is confirmed with EDS micro-chemical analysis.

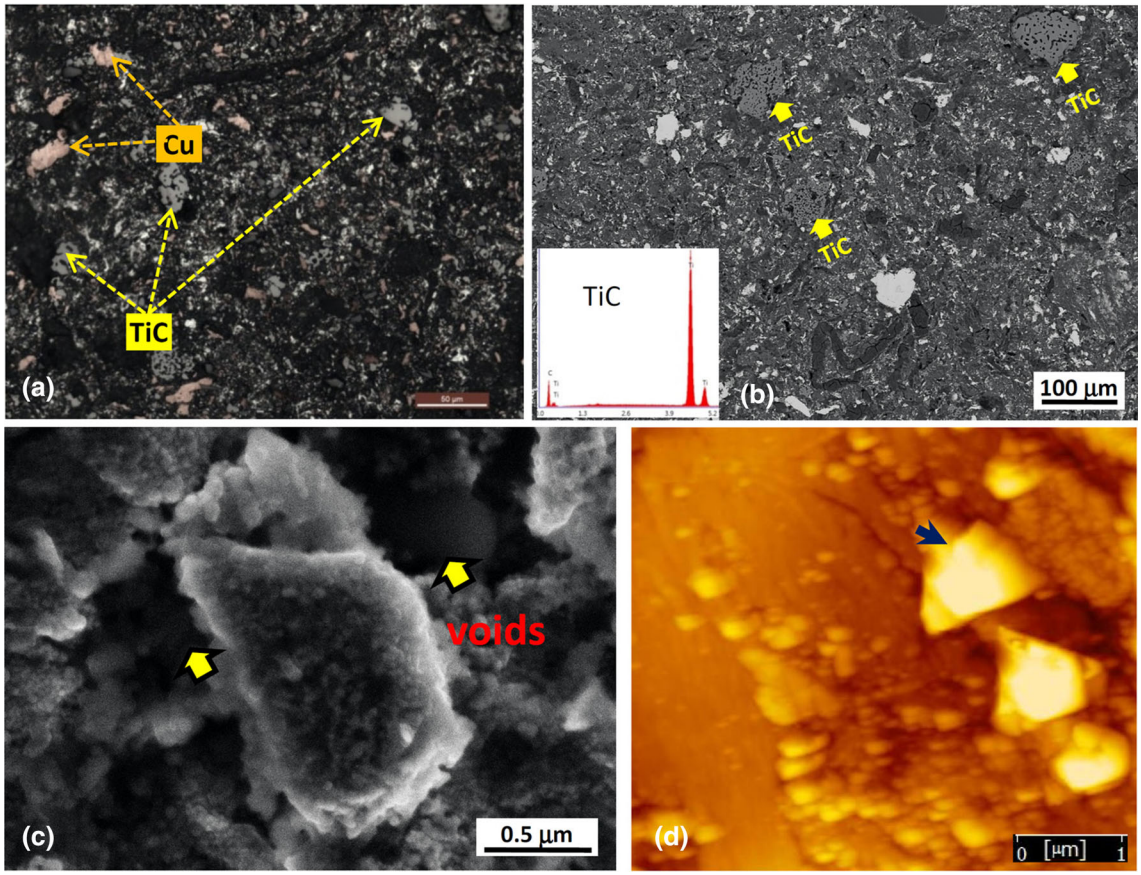

Fig. 5 (a) Optical micrograph, (b) BSE image showing the development of microstructure in SRT-10 composite. (c) Presence of voids at the TiC–matrix interface. (d) AFM image revealing the distribution of particles and particle–matrix interfaces. (b)-inset: a representative EDS pattern of a TiC particle

Figure 6 summarizes the microstructural characterization of (Al+ 27 wt.% Cu) + 5 wt.% SiC + 5 wt.% TiC (HYB-5) composite. The optical microstructure of the composite exhibits a uniform distribution of ex-situ SiC and TiC particles (Fig. 6a). The ceramic reinforcements could be identified from unique angular morphology for SiC particles and equiaxed morphology for TiC particles in the optical micrograph. In a back-scattered SEM image, along with some very coarse ceramic reinforcements, the presence of very fine phases is detected in the matrix. Brighter contrast of the particles indicates that they are Cu-rich phases, possibly some Al-Cu-based intermetallic phases. Some porosity associated with very coarse TiC particle clusters is observed in the microstructure. AFM micrograph also exhibits the clusters of the very fine secondary phases along with SiC and TiC reinforcement particles (Fig. 6c). Representative EDS patterns from the metallic and ceramic reinforcement particles are shown in Fig. 6d, indicating the micro-chemical characteristics of the phases. The FESEM micrograph and the corresponding elemental mapping (Fig. 7) exhibit the distribution of metallic Cu and other reinforcements in the matrix. The presence of very coarse TiC particle clusters could be easily detected in an otherwise uniform and fine distribution of SiC and TiC reinforcements. Bimodal distribution of metallic Cu is further evident from the Cu elemental map. A comparison of both Al and Cu maps indicates that very fine Cu-rich particles also contain Al in them, implying that these fine particles are Al-Cu-based intermetallics phases.

The constituent phases of the composites used in the present study are further confirmed by X-ray diffraction (XRD) analysis. The representative XRD patterns of SPS-compacted pure aluminum and three composites are shown in Fig. 8. It is evident from the XRD patterns of the composites that the SPS-compacted composites contain the externally added constituents (metallic Cu, SiC, TiC) in the aluminum matrix. Some trace amounts of intermetallics (such as Al_2Cu, $AlCu_3$ phases) could also be detected. This indicates that our goal of fabricating aluminum matrix composites with multiple reinforcements has been successfully achieved without the formation of deleterious phases.

3.1.1 Transmission Electron Microscopy (TEM). The effect of incorporating metallic and ceramic reinforcements on the matrix has been evaluated through transmission electron microscopy. Figure 9 summarizes the substructural evolution of aluminum in the vicinity of reinforcements. At the vicinity of metallic Cu particle, very fine nano-scale precipitate phase (presumably Al_2Cu phase) has been observed (Fig. 9a). However, very little or no dislocation sub-structure could be noticed there. On the other hand, a significantly higher dislocation network could be detected near the ceramic reinforcements in the SRS-10 composite (Fig. 9b) as well as the HYB-5 hybrid composite (Fig. 9c). It is evident that the HYB-5 composite displays the highest dislocation sub-structure among the samples studied here. A tangled dislocation network bound by low-angle grain boundaries can be seen in the

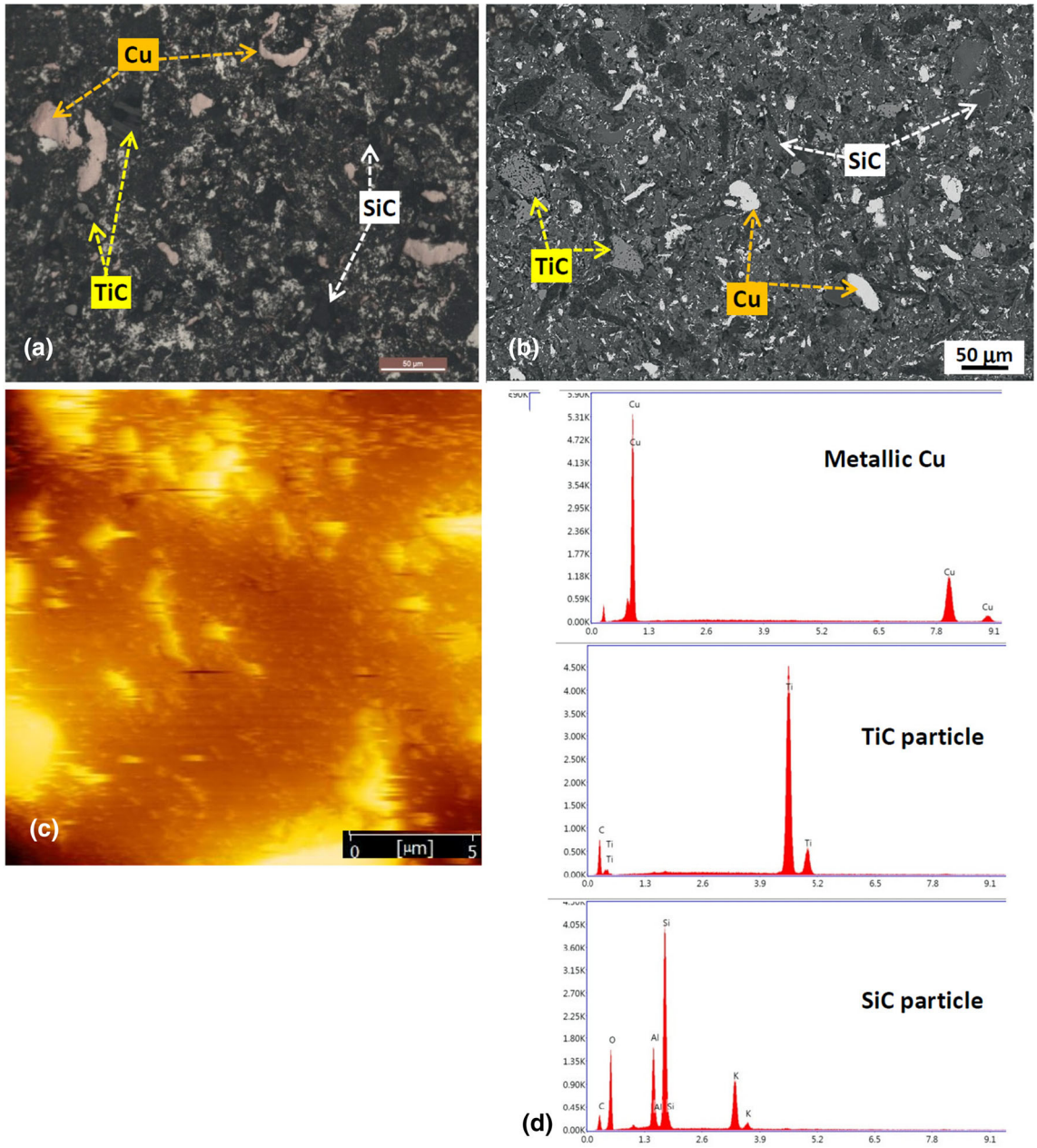

Fig. 6 (a) Optical micrograph, (b) BSE image showing the development of microstructure in HYB-5 composite. (c) AFM image revealing the distribution of particles and particle–matrix interfaces. (d) a collage of representative EDS patterns of metallic Cu, TiC, and SiC reinforcement particles

aluminum matrix of the HYB-5 sample. A comparison may be drawn to the dislocation sub-structure formation of the SPS-compacted pure aluminum sample shown in Fig.2c. An attempt has been made to quantify the dislocation density of the matrix aluminum from the TEM imaging following the Smith–Guttman linear intercept method (Ref 21). The results are reported in Table 1. In corroboration with the bright-field TEM imaging, HYB-5 displays the maximum dislocation density followed by the SRS-10 specimen. It is also noteworthy that the SPS-consolidation technique generates copious dislocation density in pure aluminum. In addition to the generation of dislocation sub-structure, the dislocation pinning effect by the very fine particles has been observed in the HYB-5 specimen (Fig. 9d). Such pinning effect of dislocations further contributes to the dislocation density of the hybrid composite.

Further high-resolution imaging using HRTEM shows the presence of copious dislocations as revealed through the inversed fast Fourier transform (IFFT) image (Fig. 10). The lattice-resolved HRTEM micrographs of SPS-compacted pure Al (Fig. 10a) and HYB-5 (Fig. 10b) demonstrate the differential dislocation generation at the ceramic particle interface. As an example, a network of interfacial dislocation is marked around the SiC particle (by the broken line). The dislocation-enriched microstructures at the vicinity of ceramic reinforcements

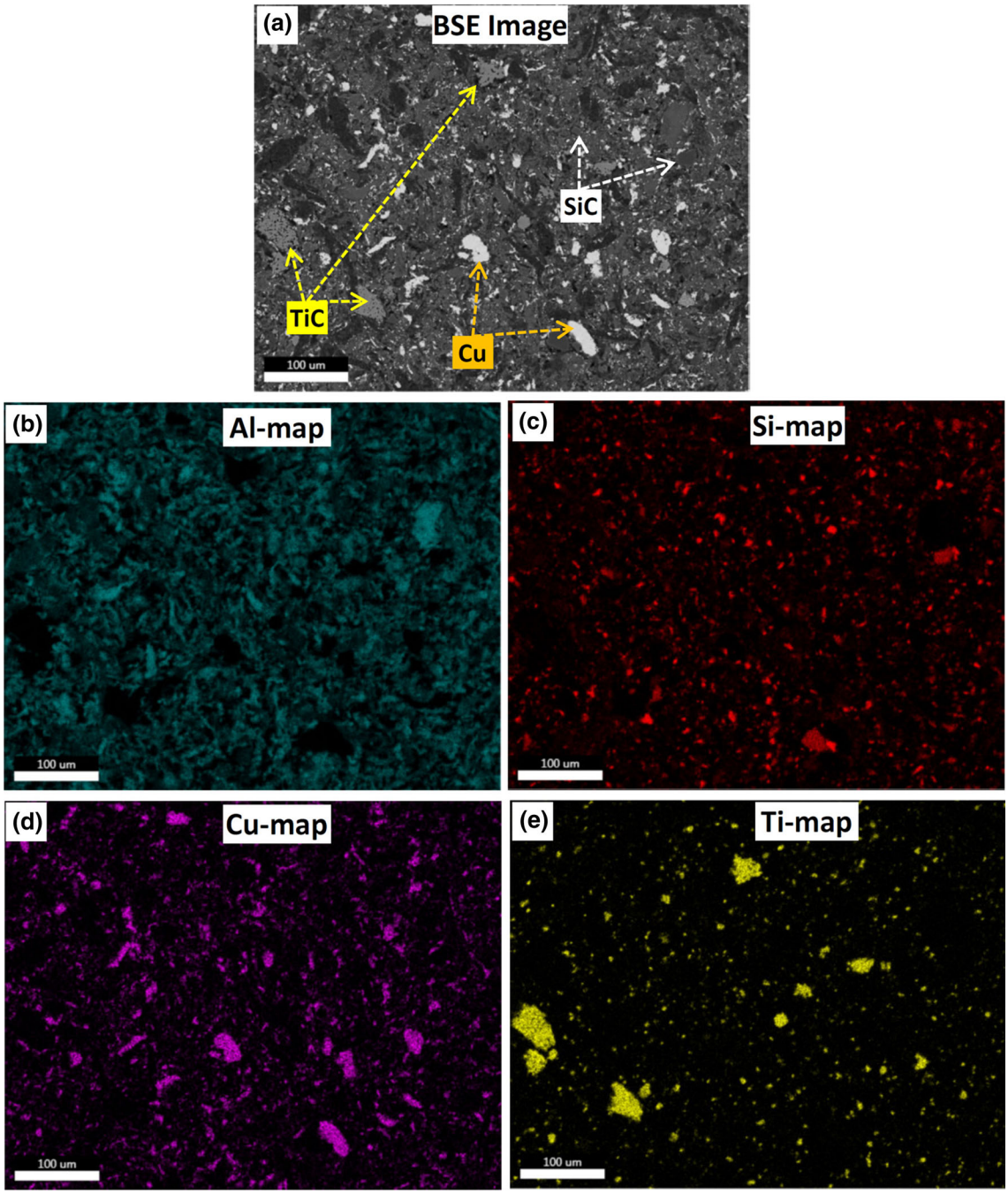

Fig. 7 (a) BSE image of the HYB-5 composite and (b)-(e) corresponding elemental maps of Al, Si, Cu, and Ti, respectively

indicate that the dislocations are generated due to the thermal mismatch between the matrix and the ceramic reinforcement.

3.2 Mechanical Properties

Mechanical properties of the composites have been evaluated by hardness testing. Vicker's hardness values of all the samples are listed in Table 1. The improvement of the bulk hardness (117 VHN) of SRS-10 compared to unreinforced aluminum (59 VHN) is attributed to the combined dispersion hardening effects of SiC particulates, metallic Cu reinforcement, and minor amounts of interfacial reaction products (e.g., Al_2Cu, $AlCu_3$). The maximum hardness has been found for the HYB-5 sample to the tune of 130 VHN. Further, the effectiveness of the strength values achieved for the present composite materials (as indicated by hardness) can be better visualized by the specific hardness values (i.e., hardness/density). Based on the experimental density of the composites, the specific hardness values are tabulated (Table 1). The specific hardness values of the HYB-5 (35.1 VHN/gcm^{-3}) and SRS-10 (32.5 VHN/gcm^{-3}) composites are considerably higher than the specific hardness of unreinforced Al (22 VHN/g cm^{-3}). Although the addition of 10 wt.% of TiC particulates causes improvement of the bulk hardness (78 VHN) compared to unreinforced Al (59VHN), the specific hardness values are similar to the unreinforced Al. This can be attributed to the

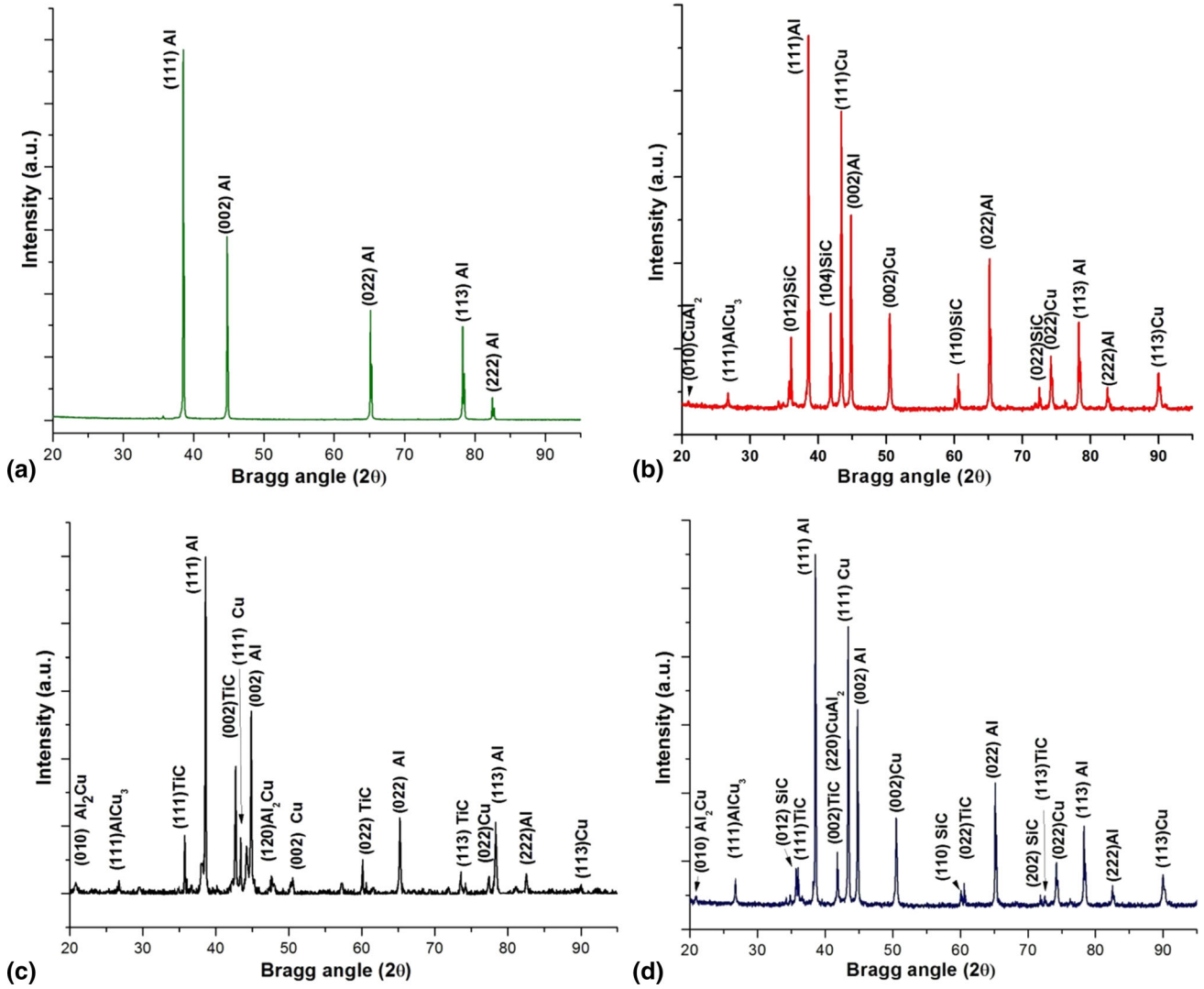

Fig. 8 Representative XRD patterns of (a) SPS-compacted Al, (b) SRS-10, (c) SRT-10, and (d) HYB-5 composites

relatively higher density of the TiC particles and thereby increasing the overall density of the composite.

3.2.1 Depth-sensing Nano-indentation Tests. Depth-sensing nano-indentation experiments have been conducted on SPS-compacted Al and HYB-5 hybrid composite to examine the indentation response of different micro-constituent phases present in the composite microstructure. The relevant plots of load (P)–penetration depth (h) for pure Al and HYB-5 samples are shown in Fig. 11(a-b). The load versus displacement curve (shown in Fig.11a) for unreinforced pure Al is typical of a ductile material with an average indentation depth of 5184 ± 208 nm at an applied load of 300 mN. For the hybrid composite, the load (force) versus penetration depth (P–h curves) curves are further generated for different microstructural regions/micro-constituents like SiC/TiC particles, matrix, and interfacial regions at an applied load of 80 mN. For particles or particle-enriched regions, the P–h curves are shallower, which is just opposite to deeper penetration depth at the matrix (Fig.11b). The parameters extracted from the P–h curves corresponding to the matrix of SPS-Al and HYB-5 samples are listed in Table 2. On an average, the hybrid composite matrix exhibits improvement in Young's modulus, Bulk modulus (Y = 96 ± 12 GPa, K= 80 GPa), and hardness (H= 75 ± 8 VHN) as compared to pure Al compact (Y= 77 ± 9 GPa, K= 64 GPa, and H= 59 ± 6 VHN).

4. Discussion

It is quite evident from the results presented in the preceding section that the SPS technique can effectively be utilized for the fabrication of tailor-made-design-based hybrid composite with various combinations of metallic (pure Cu) and ceramic reinforcements (SiC and TiC) using powder metallurgy route. This is exemplified by the low level of porosity and absence of any significant interfacial reaction product in the synthesized composites. Indeed, these two prime limitations (porosity and interfacial reaction product) of the otherwise successful ingot metallurgy route, while introducing multiple reinforcements in the matrix Al, have been successfully overcome in the present research work. In this regard, a complete reaction of TiC with aluminum alloy melt is observed in a recent research work (Ref 22) while incorporating TiC together with SiC through the ingot metallurgy route.

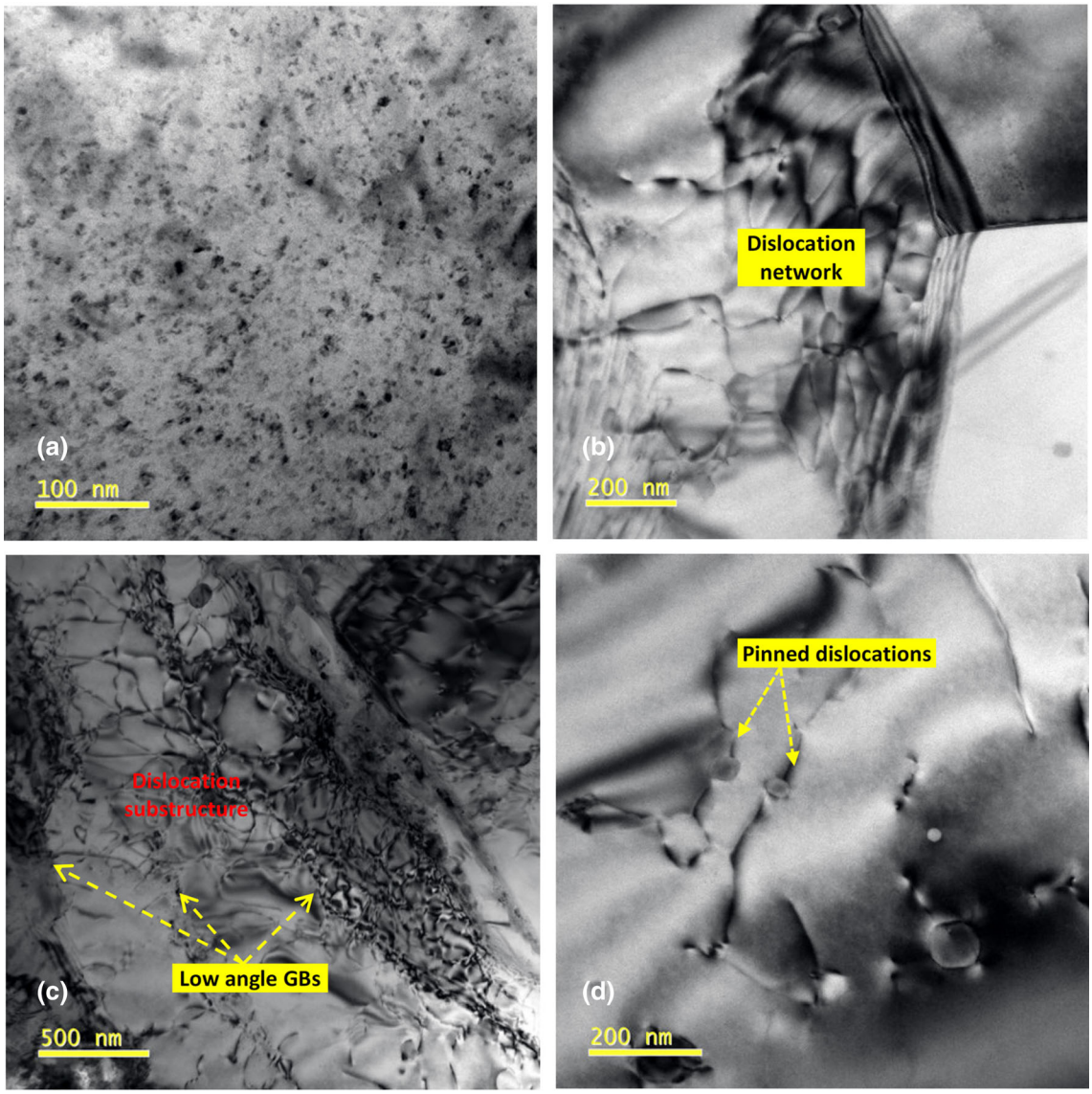

Fig. 9 Bright-field TEM images showing the development of the dislocation structure of the composites

4.1 Density and Porosity

The difference between the experimental densities and the theoretical density values predicted based on the rule of mixtures is low as the experimental density values are very close to the predicted values (Table 1). The results indicate that the SPS technique can successfully be applied to consolidate the composites having multiple types of reinforcements. The difference in density values is attributed to the presence of a minor fraction of porosities. The quantitative estimation of porosities in the composites is tabulated in Table 1 using the following formula:

$$\%\text{Porosity} = \frac{\left(\rho_{th} - \rho_{\exp}\right)}{\rho_{th}} \times 100.$$

It can be noticed that all the samples except SRT-10 show very low levels of porosity. For the SRT-10 sample, very coarse and clustered lumps of TiC particles are found to hamper the compaction and some nominal porosity (~5%) has been found near these coarse particles. The results also indicate that for a given mass fraction of reinforcement particles, the nature of particles significantly affects the porosity. It has been widely reported that during the fabrication of the particulate MMCs, the formation of porosity is a commonly observed phenomenon. It is due to the long particle feeding time and poor wettability of ceramic reinforcements (Ref 23-25) as reported for the spray-deposited Al-Cu/11% SiC composite having 6.9% porosity (Ref 25). Porosity has also been shown to increase with the increase in volume fraction and the presence of multiple types of reinforcements in the metallic matrix (Ref 24, 25). It is worth noting that a comparable level of porosity in a particulate composite with a similar fraction of reinforcements is achieved with additional thermal processing such as hot extrusion (viz., 1.7% porosity in Al/Fe+Ti hybrid composite fabricated by melt-deposition followed by hot extrusion (Ref 14), 1.2% porosity in AA1050 Al/8% SiC composite (Ref 25)). In any case, the maximum level of porosity observed in the present research work considering all synthesized composites is still not so significant (~5%), which at its basic origin appears as the clustering of voids at the particle–matrix interface (Fig. 5c) with a relatively smaller size (~ 1 μm).

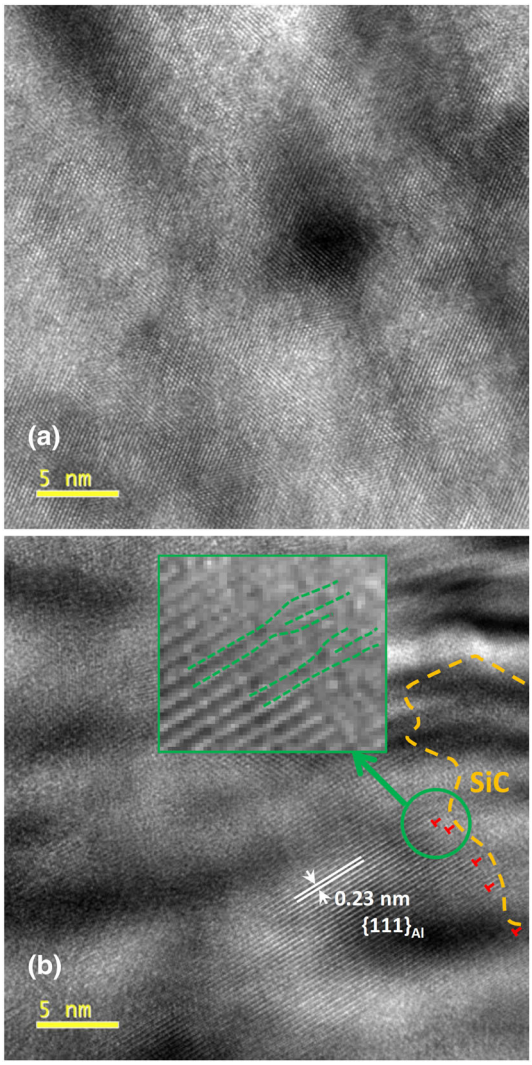

Fig. 10 High-resolution IFFT images showing (a) the relative dislocation-free Al matrix, (b) interfacial dislocations at the particle–matrix interface of hybrid composite HYB-5. Inset-(b): expanded view of the image showing the position of dislocations

4.2 High Specific Hardness and Specific Modulus

It is evident from the results presented in Table 1 that the spark plasma-sintered Al-based SiC or TiC-reinforced composites and composite with hybrid reinforcement offer significantly high specific hardness values. In addition to the bulk hardness, an attempt has been made to estimate the modulus values of the composite by nano-indentation of the constituent microstructural features. The bulk modulus of hybrid composite is obtained by applying the rule of mixture as given by the following relationship.

$$E_{HYB} = v_m E_m + v_{Cu} E_{cu} + v_{SiC} E_{SiC} + v_{TiC} E_{TiC} \quad \text{(Eq 1)}$$

where v_i *and* E_i are the volume fraction and Young's modulus of the constituent i (i: matrix Al, SiC, and TiC), respectively. The individual modulus values of the constituent phases have been calculated from the unloading curves of the nano-indentation experiments according to the procedure laid down by Doerner and Nix (Ref 26). The experimentally obtained values are compared with the theoretical values obtained by the rule of mixtures as shown in Fig. 12. It is evident from the plot the experimental values are significantly higher than those predicted by the rule of mixture. The increase in the mechanical properties of the hybrid composite is attributed to the following microstructural factors.

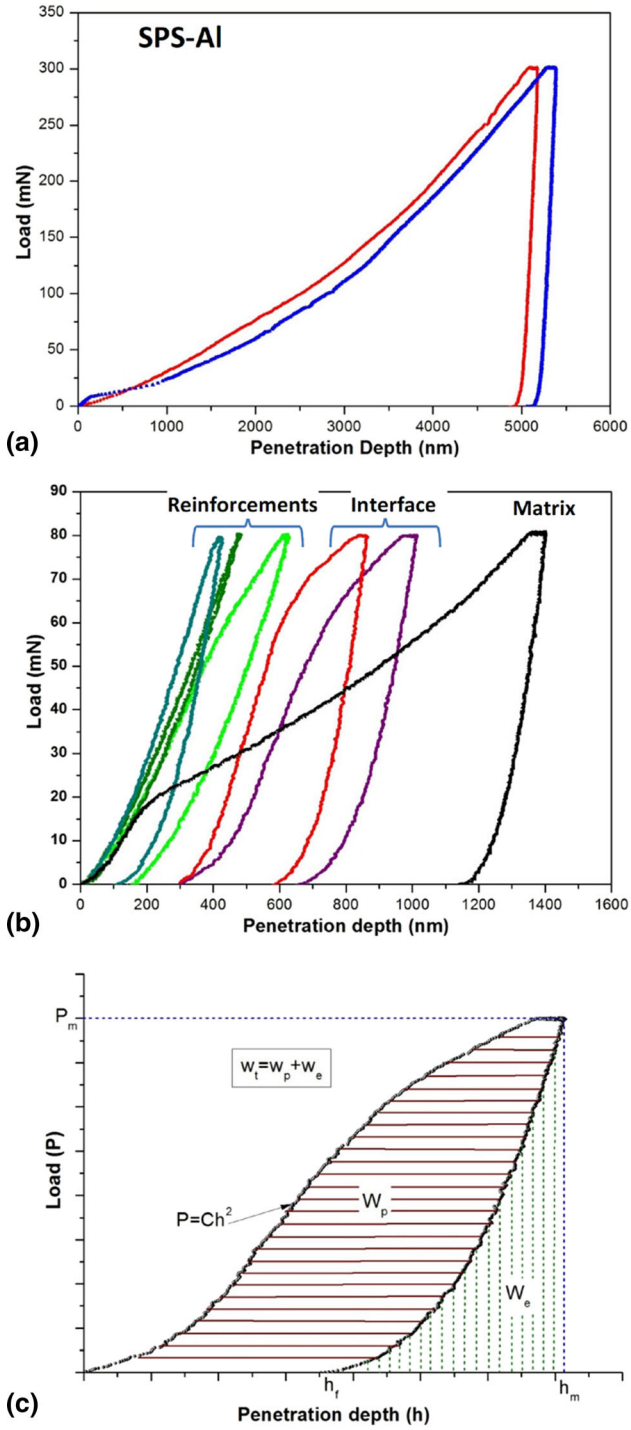

Fig. 11 The representative load (P)-penetration depth (h) curves for (a) SPS-compacted pure Al, (b) matrix, particle, and particle–matrix interfacial regions of HYB-5 composite. (c) A schematic representation of various parameters extracted from the P–h curves

(1) *Mismatch of the coefficient of thermal expansion (CTE)*: In Al-based metal matrix composites, the generation of

Table 2 Parameters obtained from experimental load (P)–penetration (h) curves

Sample ID	Maximum Penetration, h_m, nm	Residual Penetration, h_r, nm	Maximum Load, P_m, N	Reduced Modulus, E*, MPa	$S = \frac{\partial P}{\partial h}\big\|_{h=h_m}$, mN/nm
Pure Al-SPS matrix	5184	4919	0.3	77143	2.472
HYB-5 matrix	1402	1178	0.08	96412	1.956

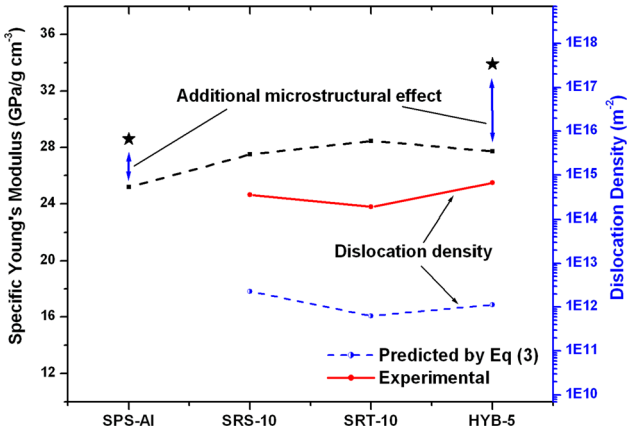

Fig. 12 A plot showing a comparison between the experimentally found Young's modulus and the one predicted by the rule of mixture. The experimentally found dislocation density and the predicted density by Eq 3 for all the composites are superimposed on the plot

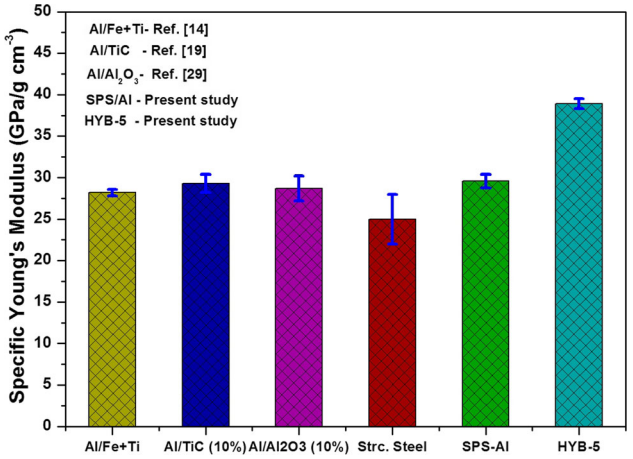

Fig. 13 A bar chart showing the superior modulus values of the HYB-5 composite in comparison with other hybrid composite and structural steel

lattice strain and dislocations are caused by the difference in the coefficient of thermal expansion (CTE) between matrix Al (CTE of Al~ 22×10^{-6} /°C) and ceramic reinforcing particles (CTE of SiC= $4.3\text{-}5.6\times10^{-6}$ /°C, CTE of TiC =$7.4\text{-}8.6\times10^{-6}$ /°C (Ref 27)). Different types of constituents (combinations of metallic and ceramic) have been added so as to generate a matrix enriched with defects (i.e., dislocation sub-structure) by virtue of the wide difference in CTE between the matrix and the reinforcements. It is evident that for a composite with the hybrid reinforcement, the mismatch is the strongest. This is well corroborated with the bright-field TEM study (Fig. 10) and the higher measured hardness.

(2) *Adequate consolidation and clean interface*: Clean particle–matrix interface without significant void and deleterious brittle intermetallic phases are visible in the AFM images (Fig. 6c), ensuring better particle–matrix bonding in hybrid composite (HYB-5) compared to composite with single reinforcement (SRS-10 and SRT-10). This is in support of the superior mechanical property of the hybrid composite.

(3) *Milling and SPS-induced defect generation*: Mechanical milling of Al and Cu powder mixture is associated with an increase in lattice strain. The increase in lattice strain is characterized by the formation of dense dislocation networks resulting in high dislocation density, as shown in Fig. 9(b,c). Further consolidation by the SPS technique retains the defect structure with minimal dynamic recovery effect as observed by several prior studies (Ref 28-30). Even the fast heating and cooling rates during the consolidation of pure aluminum cause an increase in dislocation density (Fig. 2c). The measured dislocation density values (shown in Table 1) further substantiate the experimental findings. It can be noticed that the maximum hardness values of the hybrid composite are coincident with the highest dislocation density.

Most importantly, in view of the preceding discussion, it is evident that the novel hybrid composite exhibits impressively high specific hardness (35 VHN/g cm^{-3}), specific Young's modulus (33.9 GPa/g cm^{-3}), and very high bulk modulus (28.2 GPa/g cm^{-3}) when compared with the reported range of specific hardness (13-89 VHN/g cm^{-3}) and specific Young's modulus (24-27 GPa/g cm^{-3}) and specific bulk modulus (20-22.5 GPa/g cm^{-3}) of various steels. A comparison is made with the other composites with similar levels of reinforcements and shown in Fig. 13. The superior value exhibited by the hybrid composite synthesized in the present study is distinctly evident.

4.3 Evolution of Dislocation Density

As mentioned previously, the thermal expansion coefficient (CTE) of the matrix differs significantly from that of the reinforcement and thermal fluctuation that occurs during the processing of the composite leads to the generation of thermal stresses in the aluminum matrix. The thermal stresses so generated are partly released by the generation of punched-in dislocations in the vicinity of the particle–matrix interface. Arsenault and Shi (Ref 31) have predicted the generation dislocation density using the model based on prismatic punching of dislocations at the ceramic reinforcement interface. The generation of dislocation density at the interface is given by Eq 2

$$\rho = \frac{B\Delta\alpha.\Delta T(v_i)}{bd(1-v_i)} \quad \text{(Eq 2)}$$

where B is a geometric constant (its value depends on the aspect ratio of the particles; B = 4-12 for whisker to equiaxed shapes), ΔT is the thermal fluctuation, Δα is the CTE mismatch between reinforcement and matrix, v_i is the volume fraction of the reinforcement, b is the Burgers vector, and d is the average size of reinforcement particles. For the present study, the dislocation density for the hybrid composite can be rewritten as Eq 3.

$$\rho = \frac{B\Delta\alpha.\Delta T(v_{Cu}+v_{SiC}+v_{TiC})}{bd\{1-(v_{Cu}+v_{SiC}+v_{TiC})\}} \quad \text{(Eq 3)}$$

The CTE of the composite can be predicted by a simple rule of mixture [32], given by the following relationship.

$$\alpha_{HYB} = v_m\alpha_m + v_{Cu}\alpha_{cu} + v_{SiC}\alpha_{SiC} + v_{TiC}\alpha_{TiC} \quad \text{(Eq 4)}$$

Based on the aforementioned relationships, the generation of dislocation density has been predicted for all the composites. Figure 12 compares the experimentally obtained dislocation density with those predicted by Eq 3. It can be noticed that although the trend in the variations of the experimentally obtained dislocation density with the reinforcement combinations closely follows the predicted one, the absolute magnitude of the dislocation density predicted by Eqn 3 grossly underestimates the actual dislocation density generations. The apparent discrepancy can be attributed to the two main factors. Firstly, the CTE of the composites with different types of reinforcements is relatively difficult to predict by a simple model (such as the rule of mixture) as the interaction of the different types of reinforcements with different bonding characteristics could significantly alter the internal structure of the composite. Hence, the application of the rule of mixture to estimate the CTE of the composite could be considered as a lower bound. Incorporation of hybrid reinforcements itself could create higher dislocation density. Secondly, in the present study, the dislocation density has been measured at the close vicinity of the reinforcement particles. It is known that the generation of dislocation at the particle–matrix interface due to CTE mismatch gradually fades away from the interface. On the contrary, the model predicts the average dislocation density of the composite. It is noteworthy that although the ROM is used to predict many properties such as density, Young's modulus, hardness, and sometimes a reasonable accuracy in the prediction is achieved, a similar approach to ascertain the CTE of the hybrid composite, and in turn, the calculation of dislocation density (as adapted by Prasad et al. (Ref 32)) is restricted to a merely theoretical consideration without any experimental verifications. Such a simple approach to estimate dislocation density particularly for the composites with hybrid reinforcements appears to be inadequate due to the effect of the difference of CTE at different types of particle–matrix interfaces and their final cumulative effect on the generation of dislocations. In accordance, for the hybrid composites, in particular, the experimentally measured dislocation density at the matrix region in the vicinity of the particle–matrix interface by the Smith–Guttman line intercept method has been found to be much higher than that predicted by the approach adopted by Prasad et al. (Ref 32). This signifies that a significant interactive effect of the difference in CTE exists in hybrid composites that shoots up the dislocation density to a considerably higher level. Furthermore, the pinning effect of the fine Al_2Cu, $AlCu_3$ intermetallic particles (as shown in Fig. 9d) could also contribute to the deviation of experimental dislocation density compared to the predicted ones.

4.4 Elasto-Plastic Characteristics by "The Reverse Analysis"

The experimentally measured parameters of nano-indentation on SPS-Al and HYB-5 samples indicate the elasto-plastic characteristics of the constituent components (Table 2). The ratio of elastic to plastic depth, given by the relationship $\mathbf{b = (h_m - h_r)/h_r}$, is an important parameter evaluated through nano-indentation. It can be observed from the calculated values of the parameter '**b**' that the composite with hybrid reinforcement shows much higher values (average **b**= 0.66) compared to unreinforced Al (**b**=0.03). It can be inferred that a lower value of the $(h_m - h_r)/h_r$ ratio (i.e., b value) for a higher residual penetration depth (h_r) translates into a larger plastic strain. With the increase in hybrid ceramic particle content (SiC+TiC), the ratio of elastic to plastic depth $\mathbf{b = (h_m - h_r)/ h_r}$ increases.

Further analysis of the elasto-plastic characteristics of the materials in terms of yield strength (σ_y), work hardening exponent (n), effective modulus (E*) can be obtained by the so-called reverse analysis (Ref 33) using the parameters extracted from the experimental P-h plots. Following the procedure (please refer to annexure-I) described by Prof. Suresh and co-workers (Ref 33, 34) and the experimental data from Table 2, the strain-hardening exponent (n) and yield strength (σ_y) of matrix phase of SPS-Al and HYB-5 hybrid composite can be predicted. The estimated values of n and σ_y for the SPS-Al matrix are found to be 0.382 and 97.54 MPa, while the values for the HYB-5 composite matrix are 0.304 and 112.72 MPa. It is to be noted that the hybrid composite matrix retains the strain-hardening characteristics of the unreinforced matrix to a significant extent. The relatively high magnitude of the strength and work hardening parameters stems from the empirical relations used to model the stress–strain curve of Al (i.e., $\sigma = K\varepsilon^n$) which is likely to overestimate as per standard literature, though providing some overall idea [35]. Nevertheless, such an observation reflects the success of the fabrication methodology to avoid the formation of deleterious constituents in the matrix despite incorporating a significant amount of metallic and ceramic reinforcements.

5. Conclusions

(i) A novel aluminum-based hybrid composite, with two hard ceramic reinforcing particles (5 wt.% SiC and 5 wt.% TiC) and 27 wt.% Cu as the metallic reinforcement has been successfully synthesized through a typical powder metallurgical route of a combination of ball milling and spark plasma sintering.

(ii) The synthesized composite exhibits an adequate consolidation with marginal porosity and a clean particle–matrix interface, ensuring better particle–matrix bonding. Furthermore, the evolution of dislocation in the matrix

is readily evident owing to the mismatch in the coefficient of thermal expansion.

(iii) Among the synthesized composites, the hybrid composite possesses the highest hardness and Young's modulus. Accordingly, it exhibits significantly high specific hardness (35 VHN/gcm^{-3}), specific Young's modulus (33.9 GPa/gcm^{-3}), and very high bulk modulus (28.2 GPa/gcm^{-3}) when compared with the reported range of specific hardness and specific Young's modulus of various Al-based hybrid composites with similar levels of reinforcements and structural steels.

(iv) Achievement of such unprecedented high specific strength and Young's modulus is attributed to the evolution of a novel microstructure that consists of fine SiC, TiC, and Cu particulates in a highly sub-structured aluminum-based matrix with quite a significant dislocation density (6.6×10^{14} m^{-2}). Elasto-plastic analyses of the matrix phases of the SPS-compacted Al and HYB-5 composite indicate that hybrid composite matrix retains work hardening characteristics of the unreinforced matrix to a significant extent despite incorporating a large amount of metallic and ceramic reinforcements.

Acknowledgment

The authors would like to acknowledge the support rendered by Shri Deepak Kumar, Scientist, DMRL, for his help in carrying out scanning electron microscopy.

Appendix I: Sequential Procedure for "Reverse Analysis"

It has been shown that for ductile materials like Al the stress–strain relation can be represented by [33, 34]

$$\sigma = \begin{cases} E_\varepsilon & \sigma \le \sigma_p \\ \sigma_y\left(1+\dfrac{E}{\sigma_y}\varepsilon_p\right)^n & \sigma \ge \sigma_p \end{cases} \quad \text{(Eq 5)}$$

where ε_p, σ_y, E, n represent plastic strain, yield stress, Young's modulus, and work hardening exponent, respectively. The typical loading response (i.e., loading P-h curve) during sharp indentation generally represented by the Kick's law: $P = Ch^2$, where C is the loading curvature.

In order to estimate the characteristic parameters, Dao et al. [33] have shown that by applying the Π theorem of dimensional analysis, the constitutive relations for loading and unloading curves can be represented by

$$\Pi_1\left(\frac{E^*}{\sigma_r}, n\right) = \frac{C}{\sigma_r} \quad \text{(Eq 6)}$$

$$S = \left.\frac{\partial P}{\partial h}\right|_{h=h_m} = E^* h \Pi_2\left(\frac{E^*}{\sigma_r}, n\right) \quad \text{(Eq 7)}$$

where C is loading curvature; S is the unloading curvature at h = h_m, σ_r is the representative stress at $\varepsilon_p = \varepsilon_r$; Π_1 and Π_2 are dimensionless functions. Through an elaborate numerical simulation and calibration of indentation data, Dao et al. (Ref 33) have established that at a characteristic strain of $\varepsilon_r = 0.033$, Π_1 becomes independent of n and can be represented by

$$\Pi_1\left(\frac{E^*}{\sigma_{0.033}}\right) = \frac{C}{\sigma_{0.033}} = -1.131\left[\ln\left(\frac{E^*}{\sigma_{0.033}}\right)\right]^3 + 13.635\left[\ln\left(\frac{E^*}{\sigma_{0.033}}\right)\right]^2 - 30.594\ln\left(\frac{E^*}{\sigma_{0.033}}\right) + 29.267 \quad \text{(Eq 8)}$$

And subsequently, the Π_2 can be given by

$$\Pi_2\left(\frac{E^*}{0.033}, n\right) = \frac{S}{E^* h_m} = \left(-1.40557n^3 + 0.77526n^2 + 0.1583n - 0.06831\right)\left[\ln\left(\frac{E^*}{\sigma_{0.033}}\right)\right]^3 + \left(17.93006n^3 - 9.22091n^2 - 2.37733n + 0.86295\right)\left[\ln\left(\frac{E^*}{\sigma_{0.033}}\right)\right]^2 + \left(-79.99715n^3 + 40.5562n^2 + 9.00157n - 2.54543\right)\ln\left(\frac{E^*}{\sigma_{0.033}}\right) + \left(122.65069n^3 - 63.88418n^2 - 9.58936n + 6.20045\right) \quad \text{(Eq 9)}$$

In order to estimate the parameters expressed in Eqn. (8) & (9), further correlation of strength versus penetration depth can be invoked. The ratio of residual penetration depth (h_r) to the maximum penetration (h_m) indicates the extent of plastic deformation and work hardening through the following relationship (Ref 34).

$$\frac{\sigma_{0.29-\sigma_y}}{0.29E^*} = 1 - 0.142\left(\frac{h_r}{h_m}\right) - 0.957\left(\frac{h_r}{h_m}\right)^2 \quad \text{(Eq 10)}$$

where $\sigma_{0.29}$ corresponds to flow stress at 29% strain. The effective modulus (E*) can be estimated as

$$\frac{1}{E^*} = \frac{1-\nu^2}{E} + \frac{1-\nu_{in}^2}{E_{in}} \quad \text{(Eq 11)}$$

Utilizing the value (h_r/h_m) obtained from experimental data, the quantity ($\sigma_{0.29}$-σ_y) can be estimated from Eqn. (10). By using the calculated C value, an iterative procedure could be employed to estimate $\sigma_{0.29}$, and σ_y from the following relationship (Ref 34).

$$C = M_1\sigma_{0.29}\left\{1+\frac{\sigma_y}{\sigma_{0.29}}\right\}\left\{M_2 + ln\left(\frac{E^*}{\sigma_y}\right)\right\} \quad \text{(Eq 12)}$$

References

1. A. Muthuchamy, A.R. Annamalai, S.G. Acharyya, N. Nagaraju and D.K. Agarwwal, Microstructural and Electrochemical Behaviour of Aluminum Alloy Composites Produced Using Different Sintering Techniques, *Mater. Res.*, 2018, **21**(3), p 1980–5373. https://doi.org/10.1590/1980-5373-mr-2017-0321
2. S. Devaraj, R. Kumar and S. Sankaran, Electric Erosion Induced Microstructure and Mechanical Properties in Spark Plasma Sintered Al-4.5wt.% Cu Alloy, *Mater. Perform. Charact.*, 2016, **5**(1), p 53–65.
3. M. Saiprasad, R. Atchayakumar, K. Thiruppathi and S. Raghuraman, Consolidation of Copper and Aluminum Powders by Spark Plasma Sintering, *IOP Conf. Ser. Mater. Sci. Eng.*, 2016, **149**, 012057. https://doi.org/10.1088/1757-899X/149/1/012057
4. L.K. Singh, A. Maiti, R.S. Maurya and T. Laha, Al Alloy Nanocomposite Reinforced with Physically Functionalized Carbon Nanotubes

Synthesized via Spark Plasma Sintering, *Mater. Manufac. Processes*, 2016, **31**(6), p 733–738.
5. T. Ozben, E. Kilickap and O. Çakir, Investigation of Mechanical and Machinability Properties of SiC Particle Reinforced Al-MMC, *J. Mater. Process. Technol.*, 2008, **198**(1–3), p 220–225.
6. D. Huda, M.A. El Baradie and M.S.J. Hashmi, Metal-Matrix Composites: Materials Aspects. Part II, *J. Mater. Process. Tech.*, 1993, **37**(1–4), p 529–541.
7. D.K. Koli, Properties and Characterization of Al-Al2O3 Composites Processed by Casting and Powder Metallurgy Routes (Review), *Composites*, 2013, **2**(4), p 486–496.
8. S. Suresh, A. Mortensen and A. Needleman, *Fundamentals of Metal-Matrix Composites*, Butterworth-Heinemann, Boston, 1993
9. P.B. Pawar and A.A. Utpat, Development of Aluminum Based Silicon Carbide Particulate Metal Matrix Composite for Spur Gear, *Proc. Mater. Sci.*, 2014, **6**(6), p 1150–1156.
10. S. Rawal, Metal-Matrix Composites for Space Applications, *JOM*, 2001, **53**(4), p 14–17.
11. V.C. Srivastava and S.N. Ojha, Microstructure and Electrical Conductivity of Al-SiCpcomposites Produced by Spray Forming Process, *Bull. Mater. Sci.*, 2005, **28**(2), p 125–130.
12. M.A. Aziz, T.S. Mahmoud and A.A. Aal, Modeling and Optimizing of Factors Affecting Erosion-Corrosion of AA6063-(TiC/Al2O3) Hybrid Composites by Experimental Design Method, *Mater. Sci. Eng. A*, 2008, **486**(1–2), p 313–320.
13. J.I. Song, H.D. Bong and K.S. Han, Characterization of Mechanical and Wear Properties of Al/Al_2O_3/C Hybrid Metal Matrix Composites, *Scripta Metall. Mater.*, 1995, **33**(8), p 1307–1313.
14. M. Gupta, M.O. Lai and C.Y.H. Lim, Development of a Novel Hybrid Aluminum-Based Composite with Enhanced Properties, *J. Mater. Process. Technol.*, 2006, **176**(1–3), p 191–199.
15. K.H. Oh and K.S. Han, Short-Fiber / Particle Hybrid Reinforcement: Effects on Fracture Toughness and Fatigue Crack Growth of Metal Matrix Composites, *Compsite Sci. Technol.*, 2007, **67**, p 1719–1726.
16. J.I. Song and K.S. Han, Effect of Volume Fraction of Carbon Fibers on Wear Behavior of Al /Al_2O_3/C Hybrid Metal Matrix Composites, *Compos. Struct.*, 1998, **39**(4), p 309–318.
17. M.K. Premkumar and M.G. Chu, Al-TiC Particulate Composite Produced by a Liquid State In situ Process, *Mater. Sci. Eng. A*, 1995, **202**(1–2), p 172–178.
18. A.R. Kennedy, D.P. Weston and M.I. Jones, Reaction in Al–TiC Metal Matrix Composites, *Mater. Sci. Eng. A*, 2001, **316**, p 32–38.
19. A.E. Karantzalis, S. Wyatt and A.R. Kennedy, The Mechanical Properties of Al-TiC Metal Matrix Composites Fabricated by a Flux-Casting Technique, *Mater. Sci. Eng. A*, 1997, **237**(2), p 200–206.
20. T.W. Clyne and P.J. Withers, *An Introduction to Metal Matrix Composites*, Cambridge University Press, New York, 1993
21. C.S. Smith and L. Guttman, Measurement of Internal Boundaries in Three Dimensional Structures by Random Sectioning, *Trans. Am. Inst. Min. Metall. Eng.*, 1953, **197**, p 81–87.
22. B.K. Show, D.K. Mondal, K. Biswas and J. Maity, Development of a Novel 6351Al–(Al4SiC4+SiC) Hybrid Composite with Enhanced Mechanical Properties, *Mater. Sci. Eng. A*, 2013, **579**, p 136–149.
23. M. Kok, Production and Mechanical Properties of Al_2O_3 Particle-Reinforced 2024 Aluminium Alloy Composites, *J. Mater. Process. Technol.*, 2005, **161**(3), p 381–387.
24. V.V. Ganesh, P.K. Tan and M. Gupta, Development and Characterization of an Aluminum Alloy Containing Interconnected-Wires as Reinforcement, *J. Alloys Compd.*, 2001, **315**(1–2), p 203–210.
25. M. Gupta, F. Mohamed, E. Lavernia and T.S. Srivatsan, Microstructural Evolution and Mechanical Properties of SiC/Al_2O_3 Particulate-Reinforced Spray-Deposited Metal-Matrix Composites, *J. Mater. Sci.*, 1993, **28**(8), p 2245–2259.
26. M.F. Doerner and W.D. Nix, A Method for Interpreting the Data from Depth-Sensing Indentation Instruments, *J. Mater. Res.*, 1986, **1**(4), p 601–609.
27. Anon, *Introduction to Ceramics and Glasses, Engineering Materials Handbook*, Vol. 4, ASM International, The Materials Information Society, 1991, p 30
28. J. Ye, L. Ajdelsztajn and J.M. Schoenung, Bulk Nanocrystalline Aluminum 5083 Alloy Fabricated by a Novel Technique: Cryomilling and Spark Plasma Sintering, *Metall. Mater. Trans. A*, 2006, **37**(8), p 2569–2579.
29. P.K. Rohatgi, Metal-matrix Composites, *Def. Sci. J.*, 1993, **43**(4), p 323–349.
30. N. Saheb, Z. Iqbal, A. Khalil, A.S. Hakeem, N. Al Aqeeli, T. Laoui, A. Al-Qutub and R. Kirchner, Spark Plasma Sintering of Metals and Metal Matrix Nanocomposites: A Review, *J. Nanomaterials*, 2012, **2012**, p 983470.
31. R.J. Arsenault and N. Shi, Dislocation Generation due to Differences Between the Coefficients of Thermal Expansion, *Mat. Sci. Eng.*, 1986, **81**, p 175–187.
32. D.S. Prasad, C. Shoba and N. Ramanaiah, Investigations on Mechanical Properties of Aluminum Hybrid Composites, *J. Mater. Res. Technol.*, 2014, **3**(1), p 79–85.
33. A.E. Giannakopoulos and S. Suresh, Determination of Elastoplastic Properties by Instrumented Sharp Indentation, *Scripta mater.*, 1999, **40**(10), p 1191–1198.
34. M. Dao, N. Chollacoop, K.J. Van Vliet, T.A. Venkatesh and S. Suresh, Computational Modeling of the Forward and Reverse Problems in Instrumented Sharp Indentation, *Acta mater.*, 2001, **49**, p 3899–3918.
35. C. Mondal, A.K. Singh, A.K. Mukhopadhyay and K. Chattopadhyay, Tensile Flow and Work Hardening Behavior of Hot Cross-rolled and Peak-aged AA7010 Aluminum Alloy Sheets, *Mat. Sci. Eng. A*, 2013, **577**, p 87–100.